

Boosted Electrocatalytic N₂ Reduction on Fluorine-Doped SnO₂ Mesoporous Nanosheets

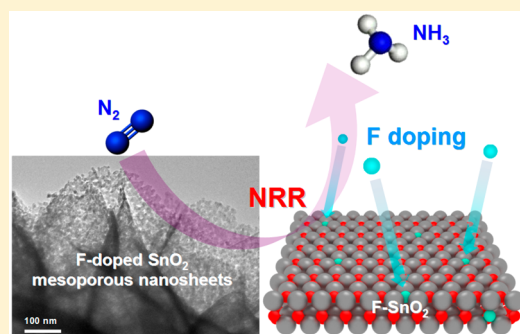
Ya-ping Liu,[†] Yu-biao Li,[†] Hu Zhang,[‡] and Ke Chu^{*,†}

[†]School of Materials Science and Engineering, Lanzhou Jiaotong University, Lanzhou 730070, China

[‡]School of Materials Science and Engineering, University of Science and Technology Beijing, Beijing 100083, China

Supporting Information

ABSTRACT: The development of highly active and durable electrocatalysts toward the N₂ reduction reaction (NRR) holds a key to ambient electrocatalytic NH₃ synthesis. Herein, fluorine (F)-doped SnO₂ mesoporous nanosheets on carbon cloth (F-SnO₂/CC) were developed as an efficient NRR electrocatalyst. Benefiting from the combined structural advantages of mesoporous nanosheet structure and F-doping, the F-SnO₂/CC exhibited high NRR activity with an NH₃ yield of 19.3 μg h⁻¹ mg⁻¹ and a Faradaic efficiency of 8.6% at -0.45 V (vs RHE) in 0.1 M Na₂SO₄, comparable or even superior to those of most reported NRR electrocatalysts. Density functional theory calculations revealed that the F-doping could readily tailor the electronic structure of SnO₂ to render it with improved conductivity and increased positive charge on active Sn sites, leading to the lowered reaction energy barriers and boosted NRR activity.



INTRODUCTION

Ever-increasing energy crisis-related and environmental pollution-related global issues have driven the urgent search for clean and sustainable energy sources. Ammonia (NH₃), as a high-efficiency and carbon-free energy carrier, is considered as a promising candidate for the future renewable energy industry.^{1,2} However, the current artificial NH₃ synthesis still dominantly depends on the energy-intensive Haber–Bosch process,³ leading to massive fossil fuel consumption and serious greenhouse gas emissions. To alleviate these issues, it is critically necessary to explore efficient and energy-saving routes for NH₃ production.

Electrocatalytic N₂-to-NH₃ conversion by the N₂ reduction reaction (NRR) provides a clean and scalable approach for NH₃ synthesis under ambient conditions.^{4–6} To realize the efficient electrocatalytic N₂ reduction, it is highly desirable to develop high-performance NRR electrocatalysts that can effectively absorb and activate N₂ molecules, facilitate the hydrogenation reaction, and simultaneously impede the competitive hydrogen evolution reaction (HER).^{7–9} To this end, a number of electrocatalysts with fascinating NRR activities in acidic/alkaline/neutral electrolytes have been recently developed, including noble metals (Ru¹⁰ and Pd¹¹), transition-metal-based oxides (Nb₂O₅,¹² TiO₂,¹³ MnO,¹⁴ and CoO¹⁵), nitrides (VN¹⁶ and MoN¹⁷), sulfides (MoS₂^{18–20}), carbides (Mo₂C^{21,22}), and metal-free materials (B₄C,²³ B nanosheets,²⁴ sulfur dots–graphene nanohybrid,²⁵ and black phosphorus²⁶).

SnO₂ is an attractive semiconductor material and has been extensively investigated in the electrocatalytic applications of lithium-ion batteries, supercapacitors, electrochemical sensing,

and fuel cells.²⁷ The very recent work reports that the SnO₂ submicrometer particles are also active for NRR with an NH₃ yield of 4.03 μg h⁻¹ mg⁻¹ and a Faradaic efficiency (FE) of 2.17%,²⁸ demonstrating the feasibility of SnO₂ for potential NRR application. Nevertheless, the NRR performance of SnO₂ submicrometer particles is far lower than the expected target, due likely to their low conductivity, limited active sites, poor N₂ adsorption, and insufficient stabilization of reaction intermediates (*N₂H, *N₂H₂, *NH₂, etc., for NRR).

Generally, the NRR performance of an electrocatalyst is largely dependent on its electronic structure, as NRR is primarily concerned with the proton-coupled electron transfer between the catalyst and N₂ molecule.²⁹ Thus, the boosted NRR activity can be achieved by rational design and engineering of the catalyst electronic structure. An effective strategy to optimize the electronic structure of the semiconductors is heteroatom doping, which can engineer the band structure and tune the electron donor–acceptor behavior,^{30–32} leading to the optimized reaction kinetics and enhanced electrocatalytic performances. Recent experimental and theoretical studies have indicated that the heteroatom doping can effectively improve the performance of semiconductor electrocatalysts toward representative energy-related electrocatalytic applications of the oxygen reduction reaction (ORR),³³ oxygen evolution reaction (OER),³⁴ HER,³⁵ and CO₂ reduction reaction (CRR).³⁶ Nonetheless, implementing the doping approach to improve the NRR performance of semiconductors is still in the infancy stage and remains largely unexplored.^{30,31}

Received: June 19, 2019

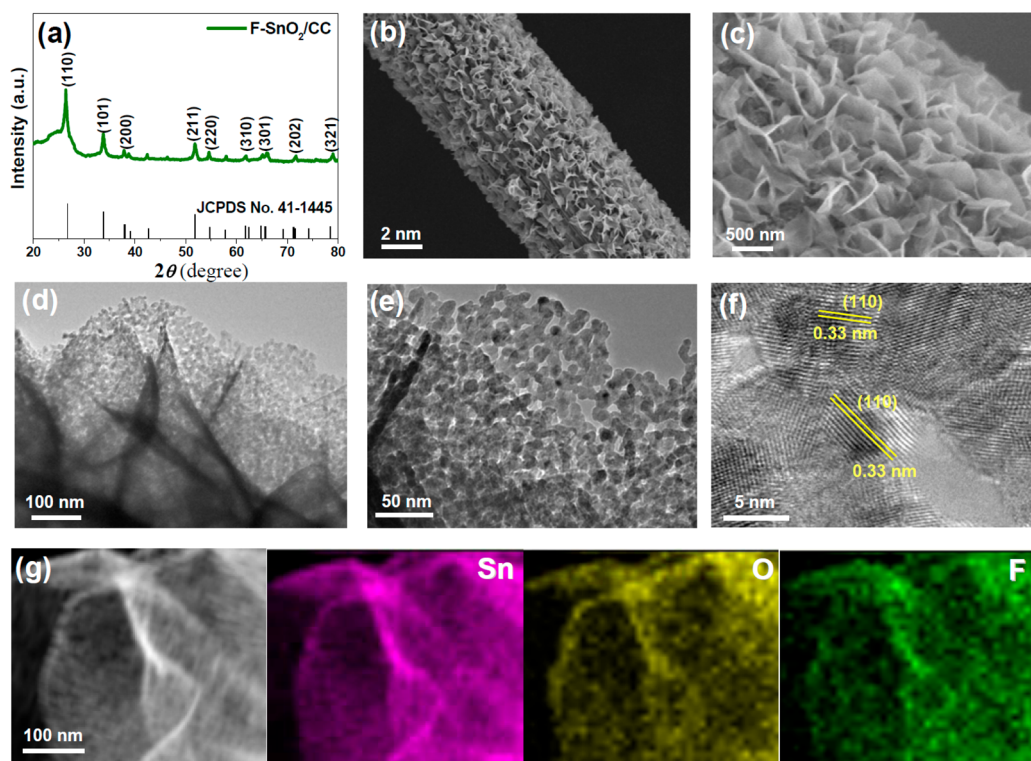


Figure 1. Characterizations of F-SnO₂/CC: (a) XRD pattern; (b, c) SEM images; (d, e) TEM images; (f) HRTEM image; and (g) HADDF-STEM element mapping images.

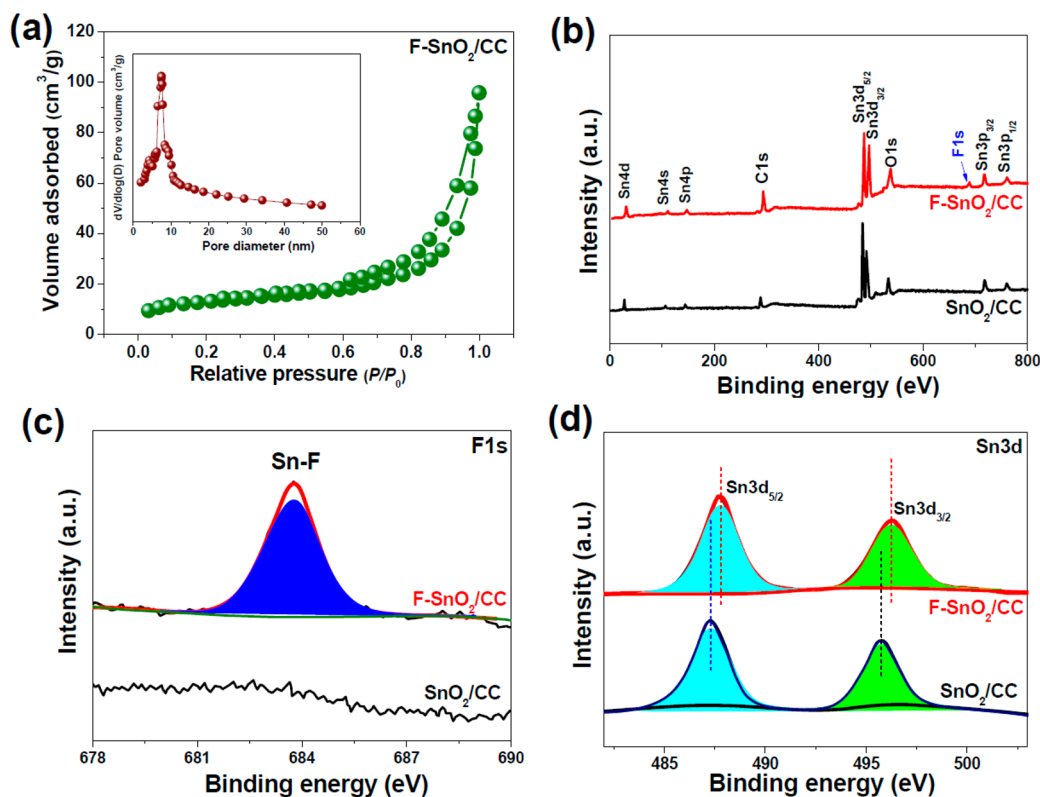


Figure 2. (a) Nitrogen adsorption/desorption isotherm curves of F-SnO₂/CC and corresponding pore size distributions (inset). (b–d) XPS spectra of SnO₂/CC and F-SnO₂/CC: (b) survey; (c) F 1s; and (d) Sn 3d.

To our knowledge, the NRR behavior of doped SnO₂, both in experimental and theoretical investigations, has not been reported to date.

Herein, the F-doped SnO₂ mesoporous nanosheets grown on carbon cloth (F-SnO₂/CC) were developed as an efficient NRR electrocatalyst. Electrochemical tests showed that the F-

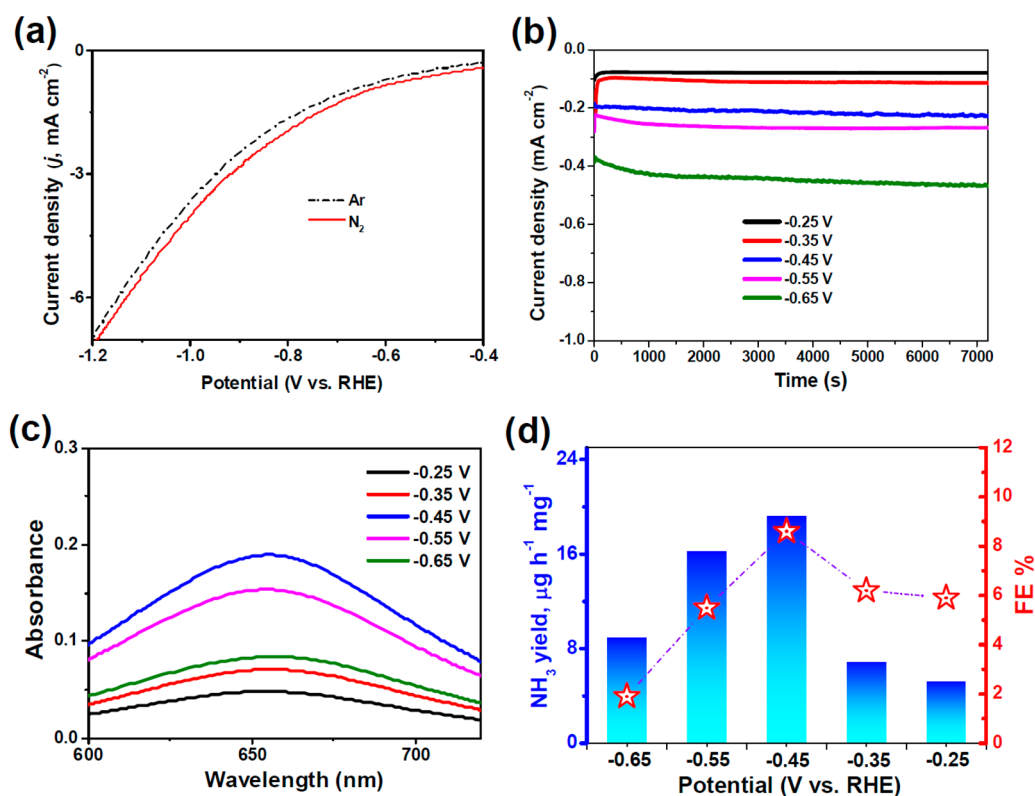


Figure 3. (a) LSV curves of F-SnO₂/CC in Ar- and N₂-saturated solutions. (b) Time-dependent current density of F-SnO₂/CC after 2 h electrolysis in N₂-saturated solution at various potentials, and corresponding (c) UV-vis absorption spectra of the electrolytes (stained with indophenol indicator) and (d) obtained NH₃ yields (columns) and FEs (stars).

SnO₂/CC exhibited an attractive NRR performance with a high NH₃ yield/FE and robust durability. Density functional theory (DFT) calculations were carried out to further gain insight into the boosted NRR activity induced by F-doping.

RESULTS AND DISCUSSION

The F-SnO₂/CC was synthesized using a facile solvothermal approach followed by calcining under air atmosphere,^{37–39} as detailed in the [Experimental Section \(Supporting Information\)](#). The X-ray diffraction (XRD) pattern of F-SnO₂/CC ([Figure 1a](#)) depicts the diffraction peaks that are indexed well to the characteristic peaks of the tetragonal SnO₂ phase (JCPDS no. 41-1445), without a second phase or precipitation. Scanning electron microscopy (SEM) images ([Figures 1b, c](#)) of F-SnO₂/CC show that the bushy F-SnO₂ nanosheets are evenly and vertically grafted on the CC surface.⁴⁰ Further structural details of F-SnO₂ nanosheets are unveiled by transmission electron microscopy (TEM) and high-resolution transmission electron microscopy (HRTEM).

Typical TEM images ([Figures 1d, e](#)) show that the F-SnO₂ nanosheets exhibit a porous structure with the existence of abundant nanopores.^{41–43} HRTEM image ([Figure 1f](#)) reflects the high crystalline structure of nanosheets with the presence of dominant (110) planes, corresponding to a specific lattice spacing of 0.33 nm. Selected area electron diffraction (SAED) pattern ([Figure S1](#)) depicts a series of diffraction rings which coincide exactly with the indexed planes of tetragonal SnO₂ as revealed by the XRD pattern ([Figure 1a](#)). High-angle annular dark-field scanning TEM (HAADF-STEM) images ([Figure 1g](#)) display the uniform distribution of Sn, O, and F elements over the F-SnO₂ nanosheets, suggesting the presence of F species in

the SnO₂ lattice. As shown in [Figure S2](#), the undoped SnO₂/CC possesses the quite similar phase structure and morphology as F-SnO₂/CC, suggesting that F-doping does not significantly alter the overall structure of SnO₂/CC.

Nitrogen adsorption–desorption measurements ([Figure 2a](#)) in terms of Brunauer–Emmett–Teller method show that the F-SnO₂/CC has a large specific surface area of 113.7 m² g⁻¹. Additionally, the pore size distribution analyzed by the Barrett–Joyner–Halenda ([Figure 2a, inset](#)) method presents a typical mesoporous structure with an average pore size of about ~7 nm, in accordance with the TEM observations ([Figures 1d, f](#)). Likewise, the undoped SnO₂/CC exhibits the similar mesoporous structures as F-SnO₂/CC ([Figure S3](#)), attributed to their morphology similarity as observed in the TEM images ([Figure 1d and f](#); [Figure S2](#)). X-ray photoelectron spectroscopy (XPS) is used to evaluate the elemental compositions and chemical structures of SnO₂/CC and F-SnO₂/CC. As depicted in [Figure 2b](#), the survey spectrum of F-SnO₂/CC exhibits C 1s, O 1s, F 1s, Sn 4s/Sn 4d/Sn 4p, and Sn 3d/Sn 3p peaks, while no F 1s can be detected in SnO₂/CC. Quantitative XPS analysis indicates the existence of 3.1 at. % F in F-SnO₂/CC.⁴⁴ In the high-resolution F 1s spectrum of SnO₂/CC ([Figure 2c](#)), the peak fitted at 683.9 eV is assigned to the formation of an Sn–F bond,⁴⁵ which is also absent for SnO₂/CC. The high-resolution XPS spectra of Sn 3d ([Figure 2d](#)) can be fitted into doublet peaks located at 487.8 and 496.2 eV, which correspond to Sn 3d_{5/2} and Sn 3d_{3/2}, respectively. Noticeably, a ~0.5 eV positive shift of Sn 3d doublet peaks is evident for F-SnO₂/CC as compared to SnO₂/CC, suggesting the electronic structure reconfiguration of F-SnO₂ due to the electron transfer from Sn atoms to F-dopants.⁴⁶ In the Raman spectra ([Figure S4](#)), the peak assigned to the A_{1g} mode of

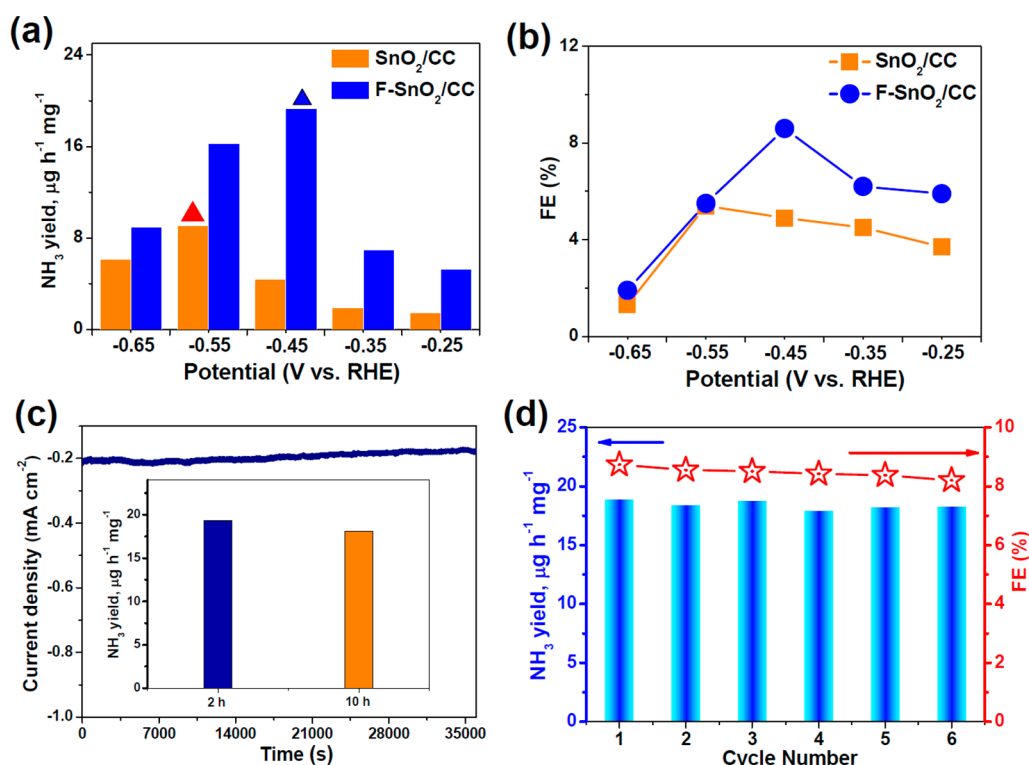


Figure 4. (a) NH₃ yields and (b) FEs of SnO₂/CC and F-SnO₂/CC at various potentials. (c) Chronoamperometry test of F-SnO₂/CC for 10 h (36000 s) electrolysis at -0.45 V, and corresponding NH₃ yield at different electrolysis times (inset). (d) Cycling test of F-SnO₂/CC for six cycles of chronoamperometric runs.

SnO₂ is found to shift to the higher wavenumber for F-SnO₂/CC relative to SnO₂/CC, which is ascribed to the surface structural disorder of SnO₂ induced by the F-doping.⁴⁷

The ambient NRR activity of F-SnO₂/CC employed as a self-supporting working electrode is examined in N₂-saturated Na₂SO₄ (0.1 M) electrolyte, using an H-type electrochemical cell (Figure S5). The indophenol blue method is used to measure the NH₃ yield and FE of generated NH₃ from NRR (Figure S6).⁴⁸ The Watt and Chrisp method⁴⁹ is applied to detect the possible N₂H₄ as a byproduct (Figure S7). As displayed in Figure S8, no N₂H₄ can be detected, which means there is a high selectivity of F-SnO₂/CC toward N₂-to-NH₃ conversion. To prove the reliability of our NRR experiment, the origination of the N source is first evaluated by isotopic labeling measurements and UV-vis analysis. After NRR electrolysis using ¹⁵N₂ as the feeding gas, it is shown in Figure S9 that the ¹H NMR spectrum presents a distinct doublet chemical shift, corresponding well to that of standard ¹⁵NH₄⁺ sample, while the characteristic ¹⁵NH₄⁺ signal is absent in the case of using Ar as the feeding gas. The same result can be obtained by using ¹⁴N₂ as the feeding gas. Likewise, as displayed in Figure S10, the NH₃ is undetectable in the controlled UV-vis tests of NRR in Ar-saturated solution, or in N₂-saturated solution at open circuit potential or in N₂-saturated solution on bare CC. Furthermore, the switching experiment (Figure S11) by conducting alternating cycling between Ar-saturated and N₂-saturated solutions reveals that the remarkable NH₃ yield is only detected in N₂-saturated solution but not in Ar-saturated solution.^{50,51} The NMR technique is also used to quantitatively determine the concentration of NRR-derived NH₃,^{21,26} and the NMR measurement (Figure S12) matches well with that attained

by the indophenol blue method. All these results prove that the detected NH₃ is solely generated from NRR catalyzing on F-SnO₂/CC.

Figure 3a shows the linear sweep voltammetry (LSV) curves of F-SnO₂/CC in Ar- and N₂-saturated electrolytes. Noticeably, a markedly higher current density is observed in N₂-saturated solution than in Ar-saturated solution, suggesting that the F-SnO₂/CC possesses NRR activity. As presented in Figure 3b, the time-dependent current densities exhibit a stable current density at various potentials over 2 h of electrolysis. Figure 3c presents the UV-vis absorption spectra of the electrolytes (stained with indophenol indicator) after 2 h NRR electrolysis on F-SnO₂/CC at various potentials from -0.25 to -0.65 V versus RHE, and the corresponding NH₃ yields and FEs are shown in Figure 3d. As seen from the results, both NH₃ yield and FE increase with increasing potential and reach their highest values at -0.45 V, being $19.3 \mu\text{g h}^{-1} \text{mg}^{-1}$ (NH₃ yield) and 8.6% (FE). Such NRR performance is comparable or even better than those of most NRR electrocatalysts reported so far (Table S1),^{52–54} demonstrating the prominent NRR activity of F-SnO₂/CC for electrocatalytic reduction of N₂ to NH₃. Nevertheless, when further increasing the potential exceeding -0.45 V, the NH₃ yield and FE of F-SnO₂/CC both decline substantially, as a result of the vigorous hydrogen evolution at elevated potentials,^{26,55} resulting in weakened N₂ adsorption and a reduced NRR activity.

For comparison, the undoped SnO₂/CC is also assessed for NRR under identical experimental conditions (Figure S13). As shown in Figure 4a and b, the SnO₂/CC presents a much lower NH₃ yield and FE than those of F-SnO₂/CC at all potentials. Specifically, the highest NH₃ yield of SnO₂/CC is $9.1 \mu\text{g h}^{-1} \text{mg}^{-1}$, less than half of that of F-SnO₂/CC ($19.3 \mu\text{g}$

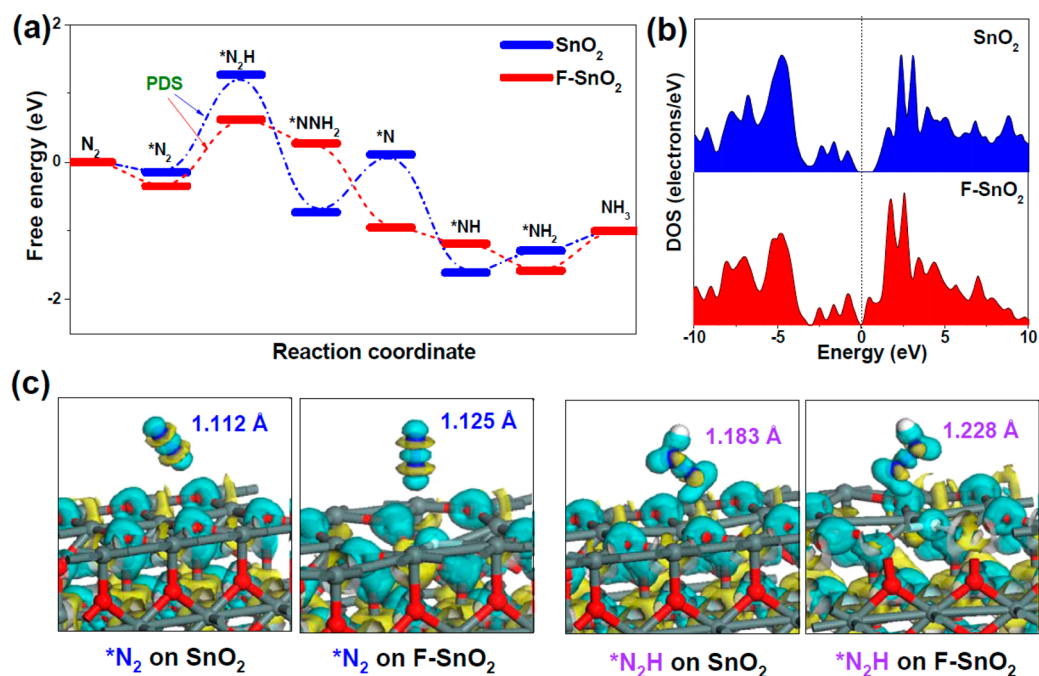


Figure 5. (a) Free energy diagrams of SnO₂ and F-SnO₂ through the distal pathway at zero applied energy. (b) Total density of states (TDOS) of SnO₂ and F-SnO₂. (c) Adsorption of *N₂ and *N₂H on SnO₂ and F-SnO₂, and corresponding N–N bond lengths and charge density distributions. Yellow and cyan regions represent the electron depletion and accumulation, respectively. Gray, red, and white spheres represent Sn, O, and F atoms, respectively.

$\text{h}^{-1} \text{mg}^{-1}$). This suggests that the F-doping can significantly improve the NRR performance of SnO₂/CC. In addition, the F-SnO₂/CC demands a lower potential of -0.45 V to attain its highest NH₃ yield and FE in contrast to -0.55 V for undoped SnO₂/CC, emphasizing the capability of F-doping to effectively decrease the NRR kinetic barrier and to promote the conversion efficiency of F-SnO₂/CC. It should be pointed out that the NRR performance of SnO₂/CC is still superior to that of reported SnO₂ submicrometer particles ($4.03 \mu\text{g h}^{-1} \text{mg}^{-1}$, 2.17%),²⁸ which can be attributed mainly to the mesoporous structure of SnO₂/CC (Figures S2 and S3). The mesoporous structure favors the exposure of abundant active sites and facilitates the transport of electrolyte/reactants and electrons, beneficial for the improved NRR activity. Furthermore, the HER activities of SnO₂/CC and F-SnO₂/CC in 0.1 M Na₂SO₄ are also evaluated. It can be found in Figure S14 that the F-doping has little impact on the HER activity and that both catalysts exhibit very poor HER performances, as evidenced by the large overpotentials ($>1.2 \text{ V}$) to achieve a current density of 10 mA cm^{-2} (Figure S14a), and high Tafel slopes ($>600 \text{ mV dec}^{-1}$, Figure S14b). The poor HER performances of F-SnO₂/CC (SnO₂/CC) results mainly from the intrinsically weak HER activity of SnO₂²⁸ and the neutral Na₂SO₄ solution in which a larger kinetic energy barrier is required to drive HER relative to acid media.³²

To further explore the improved NRR behavior F-SnO₂/CC, the electrochemically active surface areas of SnO₂/CC and F-SnO₂/CC are examined by electrochemical double-layer capacitance (C_{dl}). It is shown in Figure S15 that the F-SnO₂/CC exhibits a slightly lower C_{dl} (19.5 mF cm^{-2}) than that of SnO₂/CC (21.7 mF cm^{-2}) but a far better NRR performance (Figure 3c, d), elucidating that the enhanced NRR activity of F-SnO₂/CC does not stem from the variation in active surface area. Nevertheless, the N₂-TPD measurement (Figure S16) discloses a noticeably higher N₂ chemisorption peak for F-

SnO₂/CC relative to SnO₂/CC, demonstrating that the F-doping can effectively improve the adsorption ability of SnO₂/CC. As the initial step of the NRR process, the enhanced adsorption ability of N₂ caused by F-doping is very beneficial for acquiring the favorable NRR activity of F-SnO₂/CC.²¹ Furthermore, the electrochemical impedance spectroscopy measurements (EIS, Figure S17) show that the F-SnO₂/CC delivers a smaller charge-transfer resistance than SnO₂/CC, manifesting that the F-doping can largely enhance the conductivity of SnO₂/CC, favorable for the accelerated NRR kinetics of F-SnO₂/CC.

The stability is another critical factor affecting the practical application of a catalyst. The robust current stability of F-SnO₂/CC has been confirmed for 2 h electrolysis, as shown in Figure 3a. It is worth noting that the stable current density can also be well retained during 10 h (36000 s) electrolysis at -0.45 V (Figure 4c). After 10 h electrolysis, F-SnO₂/CC still maintains 96.1% of the NH₃ yield achieved after 2 h electrolysis, which indicates its long-term stability. In addition, when performing six cycles of chronoamperometric runs (Figure S18), the F-SnO₂/CC displays no noticeable decline in NH₃ yield and FE (Figure 4d), suggesting a prominent cycling stability. Moreover, after stability tests, F-SnO₂/CC can well-maintain its original morphologies (Figure S19), phase structure (Figure S20), and chemical compositions (Figure S21), verifying the good structural stability. The robust durability of F-SnO₂/CC stems from the strong covalent bonding of F-dopants and direct growth of F-SnO₂ nanosheets on CC with firm catalyst attachment.^{56,57} In sum, all of the above results strongly demonstrate that the F-SnO₂/CC possesses favorable NRR performance with relatively high NH₃ yield/FE, low potential, and robust durability, making it a promising efficient NRR electrocatalyst for electrochemical N₂ fixation.

DFT calculations are conducted to look into the boosted NRR activity of F-SnO₂ induced by F-doping. The (110) plane of SnO₂ is selected for structural modeling, because SnO₂ (110) possesses the lowest surface energy,⁵⁸ and it is also the dominant crystal face for the present SnO₂ as supported by the HRTEM observation (Figure 1f). The optimized geometry structures of SnO₂ and F-SnO₂ are shown in Figure S22.

The NRR kinetic pathway is first investigated based on the calculated Gibbs free energy (ΔG) diagrams. Theoretically, the associative distal pathway is proved to be more energetically preferable over an alternating pathway, because the distal pathway generally requires lower energy barriers.^{18,59} Experimentally, N₂H₄, an alternating intermediate, is undetectable after NRR electrolysis (Figure S8). Accordingly, the distal pathway is considered here for examining the formation energies of the intermediates (i.e., *N₂H, *N, and *NH₂) on the catalysts. As shown in Figure 5a, both SnO₂ and F-SnO₂ deliver the largest ΔG for *N₂H formation (ΔG_{*N_2H}) in their whole NRR pathways, suggesting the first hydrogenation reaction (*N₂ → *N₂H) to weaken the strong N≡N bond is the potential determine step (PDS). This is in agreement with the reported results and indicates that the *N₂ → *N₂H is the most difficult NRR step to drive NRR.^{14,18,22} Encouragingly, after F-doping, the N₂ adsorption and activation are considerably boosted, and ΔG_{*N_2H} is largely reduced from 1.25 eV for SnO₂ to 0.68 eV for F-SnO₂, indicating that the F-doping helps to stabilize the *N₂H and significantly promotes the initial hydrogenation reaction. After *N₂ → *N₂H, the following reaction steps of F-SnO₂ are almost downhill, while the SnO₂ needs to overcome a second high energy barrier of 0.87 eV to drive *NNH₂ → *N. Although the last step for NH₃ desorption is uphill for both SnO₂ and F-SnO₂, the generated NH₃ can be easily dissolved in water,²⁰ favoring the release of NH₃ from the catalyst surface and making *NH₂ → NH₃ still energetically efficient. Therefore, F-doping can effectively lower the reaction energy barrier and lead to a more favorable NRR kinetics of F-SnO₂. As shown in Figure S23, when the external potential exceeding PDS is applied, all the reaction steps of F-SnO₂ become downhill and NRR takes place spontaneously.

To further explore the improved NRR activity of SnO₂ achieved by F-doping, the density of states (DOS) of SnO₂ and F-SnO₂ is analyzed. As seen in Figure 5b, the SnO₂ exhibits a distinct band gap at the Fermi level and is thus semi-conducting. In contrast, F-doping can negatively shift the conduction band of SnO₂ toward the Fermi level, resulting in a definite zero band gap and metallic characteristics of F-SnO₂. The improved conductivity of F-SnO₂ is even more pronounced on its F-containing top surface with noticeable electronic states crossing the Fermi level, as revealed by the local density of states (LDOS, Figure S24). The enhanced surface conductivity is beneficial for the NRR activity of F-SnO₂ by facilitating the electron transport at the surface reactive sites and contributing to the successive N₂ reduction.²⁴

Further insights can be gained from the modulated electron donor–acceptor behavior of F-SnO₂. The Mulliken charge analysis (Figure S22) reveals that three Sn atoms (+1.11, +1.88, and +1.88 |e|), bonding directly to F-dopant, become more positive compared to those of undoped SnO₂ (+0.99, +1.79, and +1.79 |e|). This suggests the increased positive charge on Sn atoms upon replacing O with F, which is attributed to the higher electronegativity of F (3.98) than O (3.44), and F

atoms can grab more electrons from the adjacent Sn atoms. As N₂ is a weak Lewis base (negatively charged) in nature,⁶⁰ the increased positive charge on Sn atoms can enhance the electrostatic interaction between the active Sn sites and N₂, which is beneficial for the N₂ adsorption and dissociation during the NRR. As shown in Figure 5c, the predicted N–N bonds of adsorbed *N₂ and *N₂H on F-SnO₂ are elongated to 1.125 and 1.228 Å, respectively, which are lengthier than those (*N₂:1.112 Å, *N₂H:1.183 Å) achieved on SnO₂, implying that the F-SnO₂ is more favorable for N–N bond cleavage and hydrogenation reaction. Therefore, F-doping can effectively modulate the electronic structures of F-SnO₂ to render it with improved conductivity and increased positive charge on active Sn sites, leading to the reduced NRR energy barriers of the NRR process and enhanced NRR activity of F-SnO₂.

CONCLUSIONS

In summary, F-SnO₂/CC was experimentally and theoretically confirmed to be an effective and durable NRR catalyst. In 0.1 M Na₂SO₄, F-SnO₂/CC exhibited an NH₃ yield of 19.3 μg h⁻¹ mg⁻¹ and an FE of 8.6% at -0.45 V, as well as robust durability, comparing favorably to the most reported NRR catalysts. The fascinating NRR performance of F-SnO₂/CC was intimately associated with the synergetic structure advantages of the mesoporous nanosheet structure and F-doping. Specifically, DFT results unveiled that F-doping could improve the conductivity and increase the positive charge density on active Sn sites, resulting in reduced reaction energy barriers and enhanced NRR activity. This work not only highlights the heteroatom doping as an effective strategy to develop efficient semiconductor-based NRR catalyst but also deepens the understanding of the doping-related NRR mechanism.

ASSOCIATED CONTENT

Supporting Information

The Supporting Information is available free of charge on the ACS Publications website at DOI: 10.1021/acs.inorgchem.9b01823.

Experimental section: characterizations of SnO₂/CC and F-SnO₂/CC; photograph of an H-type electrochemical cell; determination of NH₃ concentration and N₂H₄ concentration; NMR tests; NRR performance of SnO₂/CC; HER performances of SnO₂/CC and F-SnO₂/CC; N₂-TPD tests; electrochemical impedance measurements; morphologies and structures of F-SnO₂/CC after stability test; additional DFT results; and comparison of NH₃ yield and Faradaic efficiency for recently reported NRR electrocatalysts (PDF)

AUTHOR INFORMATION

Corresponding Author

*E-mail: chukelut@163.com.

ORCID

Ke Chu: 0000-0002-0606-2689

Notes

The authors declare no competing financial interest.

ACKNOWLEDGMENTS

This work is supported by the National Natural Science Foundation of China (51761024, 51671022), the CAS Light of

West China Program, the Feitian Scholar Program of Gansu Province, and the Foundation of a Hundred Youth Talents Training Program of Lanzhou Jiaotong University.

REFERENCES

- (1) Sordakis, K.; Tang, C.; Vogt, L. K.; Junge, H.; Dyson, P. J.; Beller, M.; Laurenczy, G. Homogeneous Catalysis for Sustainable Hydrogen Storage in Formic Acid and Alcohols. *Chem. Rev.* **2018**, *118*, 372–433.
- (2) Wang, F.; Liu, Y. P.; Zhang, H.; Chu, K. CuO/Graphene Nanocomposite for Nitrogen Reduction Reaction. *ChemCatChem* **2019**, *11*, 1441–1447.
- (3) van Breemen, N. Nitrogen Cycle - Natural Organic Tendency. *Nature* **2002**, *415*, 381–382.
- (4) Zhao, J.; Zhang, L.; Xie, X.-Y.; Li, X.; Ma, Y.; Liu, Q.; Fang, W.-h.; Shi, X.; Cui, G.; Sun, X. Ti₃C₂Tx (T = F, OH) Mxene Nanosheet: A Conductive 2D Catalyst for Ambient Electrohydrogenation of N₂ to NH₃. *J. Mater. Chem. A* **2018**, *6*, 24031–24035.
- (5) Zhu, X.; Liu, Z.; Liu, Q.; Luo, Y.; Shi, X.; Asiri, A. M.; Wu, Y.; Sun, X. Efficient and Durable N₂ Reduction Electrocatalysis under Ambient Conditions: β -FeOOH Nanorods as a Non-Noble-Metal Catalyst. *Chem. Commun.* **2018**, *54*, 11332–11335.
- (6) Wang, T.; Xia, L.; Yang, J.-J.; Wang, H.; Fang, W.-H.; Chen, H.; Tang, D.; Asiri, A. M.; Luo, Y.; Cui, G.; Sun, X. Electrocatalytic N₂-to-NH₃ Conversion Using Oxygen-Doped Graphene: Experimental and Theoretical Studies. *Chem. Commun.* **2019**, *55*, 7502–7505.
- (7) Luo, Y. R.; Chen, G. F.; Ding, L.; Chen, X. Z.; Ding, L. X.; Wang, H. H. Efficient Electrocatalytic N₂ Fixation with Mxene under Ambient Conditions. *Joule* **2019**, *3*, 279–289.
- (8) Chen, G.-F.; Cao, X.; Wu, S.; Zeng, X.; Ding, L.-X.; Zhu, M.; Wang, H. Ammonia Electrosynthesis with High Selectivity under Ambient Conditions via a Li⁺ Incorporation Strategy. *J. Am. Chem. Soc.* **2017**, *139*, 9771–9774.
- (9) Zhang, L. L.; Chen, G. F.; Ding, L. X.; Wang, H. H. Advanced Non-Metallic Catalysts for Electrochemical Nitrogen Reduction under Ambient Conditions. *Chem. - Eur. J.* **2019**, *1* DOI: 10.1002/chem.201901668.
- (10) Kitano, M.; Kanbara, S.; Inoue, Y.; Kuganathan, N.; Sushko, P. V.; Yokoyama, T.; Hara, M.; Hosono, H. Electride Support Boosts Nitrogen Dissociation over Ruthenium Catalyst and Shifts the Bottleneck in Ammonia Synthesis. *Nat. Commun.* **2015**, *6*, 6731.
- (11) Wang, J.; Yu, L.; Hu, L.; Chen, G.; Xin, H.; Feng, X. Ambient Ammonia Synthesis via Palladium-Catalyzed Electrohydrogenation of Dinitrogen at Low Overpotential. *Nat. Commun.* **2018**, *9*, 1795.
- (12) Han, J.; Liu, Z.; Ma, Y.; Cui, G.; Xie, F.; Wang, F.; Wu, Y.; Gao, S.; Xu, Y.; Sun, X. Ambient N₂ Fixation to NH₃ at Ambient Conditions: Using Nb₂O₅ Nanofiber as a High-Performance Electrocatalyst. *Nano Energy* **2018**, *52*, 264–270.
- (13) Zhang, X.; Liu, Q.; Shi, X.; Asiri, A. M.; Luo, Y.; Sun, X.; Li, T. TiO₂ Nanoparticles-Reduced Graphene Oxide Hybrid: An Efficient and Durable Electrocatalyst toward Artificial N₂ Fixation to NH₃ under Ambient Conditions. *J. Mater. Chem. A* **2018**, *6*, 17303–17306.
- (14) Wang, Z.; Gong, F.; Zhang, L.; Wang, R.; Ji, L.; Liu, Q.; Luo, Y.; Guo, H.; Li, Y.; Gao, P.; Shi, X.; Li, B.; Tang, B.; Sun, X. Electrocatalytic Hydrogenation of N₂ to NH₃ by MnO: Experimental and Theoretical Investigations. *Adv. Sci.* **2019**, *6*, 1801182.
- (15) Chu, K.; Liu, Y.; Li, Y.; Zhang, H.; Tian, Y. Efficient Electrocatalytic N₂ Reduction on CoO Quantum Dots. *J. Mater. Chem. A* **2019**, *7*, 4389–4394.
- (16) Yang, X.; Nash, J.; Anibal, J.; Dunwell, M.; Kattel, S.; Stavitski, E.; Attenkofer, K.; Chen, J. G.; Yan, Y.; Xu, B. Mechanistic Insights into Electrochemical Nitrogen Reduction Reaction on Vanadium Nitride Nanoparticles. *J. Am. Chem. Soc.* **2018**, *140*, 13387–13391.
- (17) Zhang, L.; Ji, X.; Ren, X.; Luo, Y.; Shi, X.; Asiri, A. M.; Zheng, B.; Sun, X. Efficient Electrochemical N₂ Reduction to NH₃ on Mon Nanosheets Array under Ambient Conditions. *ACS Sustainable Chem. Eng.* **2018**, *6*, 9550–9554.
- (18) Zhang, L.; Ji, X.; Ren, X.; Ma, Y.; Shi, X.; Tian, Z.; Asiri, A. M.; Chen, L.; Tang, B.; Sun, X. Electrochemical Ammonia Synthesis via Nitrogen Reduction Reaction on a MoS₂ Catalyst: Theoretical and Experimental Studies. *Adv. Mater.* **2018**, *30*, 1800191.
- (19) Li, X.; Ren, X.; Liu, X.; Zhao, J.; Sun, X.; Zhang, Y.; Kuang, X.; Yan, T.; Wei, Q.; Wu, D. MoS₂ Nanosheet-Reduced Graphene Oxide Hybrid: An Efficient Electrocatalyst for Electrocatalytic N₂ Reduction to NH₃ under Ambient Conditions. *J. Mater. Chem. A* **2019**, *7*, 2524–2528.
- (20) Li, X.; Li, T.; Ma, Y.; Wei, Q.; Qiu, W.; Guo, H.; Shi, X.; Zhang, P.; Asiri, A. M.; Chen, L.; Tang, B.; Sun, X. Boosted Electrocatalytic N₂ Reduction to NH₃ by Defect-Rich MoS₂ Nanoflower. *Adv. Energy Mater.* **2018**, *8*, 1801357.
- (21) Cheng, H.; Ding, L. X.; Chen, G. F.; Zhang, L. L.; Xue, J.; Wang, H. H. Molybdenum Carbide Nanodots Enable Efficient Electrocatalytic Nitrogen Fixation under Ambient Conditions. *Adv. Mater.* **2018**, *30*, 1803694.
- (22) Ren, X.; Zhao, J.; Wei, Q.; Ma, Y.; Guo, H.; Liu, Q.; Wang, Y.; Cui, G.; Asiri, A. M.; Li, B.; Tang, B.; Sun, X. High-Performance N₂-to-NH₃ Conversion Electrocatalyzed by Mo₂C Nanorod. *ACS Cent. Sci.* **2019**, *5*, 116–121.
- (23) Qiu, W.; Xie, X.-Y.; Qiu, J.; Fang, W.-H.; Liang, R.; Ren, X.; Ji, X.; Cui, G.; Asiri, A. M.; Cui, G.; Tang, B.; Sun, X. High-Performance Artificial Nitrogen Fixation at Ambient Conditions Using a Metal-Free Electrocatalyst. *Nat. Commun.* **2018**, *9*, 3485.
- (24) Zhang, X.; Wu, T.; Wang, H.; Zhao, R.; Chen, H.; Wang, T.; Wei, P.; Luo, Y.; Zhang, Y.; Sun, X. Boron Nanosheet: An Elemental Two-Dimensional (2D) Material for Ambient Electrocatalytic N₂-to-NH₃ Fixation in Neutral Media. *ACS Catal.* **2019**, *9*, 4609–4615.
- (25) Chen, H.; Zhu, X.; Huang, H.; Wang, H.; Wang, T.; Zhao, R.; Zheng, H.; Asiri, A. M.; Luo, Y.; Sun, X. Sulfur Dots-Graphene Nanohybrid: A Metal-Free Electrocatalyst for Efficient N₂-to-NH₃ Fixation under Ambient Conditions. *Chem. Commun.* **2019**, *55*, 3152–3155.
- (26) Zhang, L. L.; Ding, L. X.; Chen, G. F.; Yang, X. F.; Wang, H. H. Ammonia Synthesis under Ambient Conditions: Selective Electroreduction of Dinitrogen to Ammonia on Black Phosphorus Nanosheets. *Angew. Chem.* **2019**, *131*, 2638–2642.
- (27) Jiang, L.; Sun, G.; Zhou, Z.; Sun, S.; Wang, Q.; Yan, S.; Li, H.; Tian, J.; Guo, J.; Zhou, B.; Xin, Q. Size-Controllable Synthesis of Monodispersed SnO₂ Nanoparticles and Application in Electrocatalysts. *J. Phys. Chem. B* **2005**, *109*, 8774–8.
- (28) Zhang, L.; Ren, X.; Luo, Y.; Shi, X.; Asiri, A. M.; Li, T. S.; Sun, X.-P. Ambient NH₃ Synthesis via Electrochemical Reduction of N₂ over Cubic Sub-Micron SnO₂ Particle. *Chem. Commun.* **2018**, *54*, 12966–12969.
- (29) Guo, C.; Ran, J.; Vasileff, A.; Qiao, S.-Z. Rational Design of Electrocatalysts and Photo (Electro) Catalysts for Nitrogen Reduction to Ammonia (NH₃) under Ambient Conditions. *Energy Environ. Sci.* **2018**, *11*, 45–56.
- (30) Zhu, X.; Liu, Z.; Wang, H.; Zhao, R.; Chen, H.; Wang, T.; Wang, F.; Luo, Y.; Wu, Y.; Sun, X. Boosting Electrocatalytic N₂ Reduction to NH₃ on β -FeOOH by Fluorine Doping. *Chem. Commun.* **2019**, *55*, 3987–3990.
- (31) Wang, Y.; Jia, K.; Pan, Q.; Xu, Y.; Liu, Q.; Cui, G.; Guo, X.; Sun, X. Boron-Doped TiO₂ for Efficient Electrocatalytic N₂ Fixation to NH₃ at Ambient Conditions. *ACS Sustainable Chem. Eng.* **2019**, *7*, 117–122.
- (32) Roger, I.; Shipman, M. A.; Symes, M. D. Earth-Abundant Catalysts for Electrochemical and Photoelectrochemical Water Splitting. *Nat. Rev. Chem.* **2017**, *1*, 0003.
- (33) Tsai, M. C.; Nguyen, T. T.; Akalework, N. G.; Pan, C. J.; Rick, J.; Liao, Y. F.; Su, W. N.; Hwang, B. J. Interplay between Molybdenum Dopant and Oxygen Vacancies in TiO₂ Support Enhances Oxygen Reduction Reaction. *ACS Catal.* **2016**, *6*, 6551.
- (34) Yu, M.; Wang, Z.; Hou, C.; Liang, C.; Zhao, C.; Tong, Y.; Lu, X.; Yang, S.; Wang, Z. Nitrogen-Doped Co₃O₄ Mesoporous Nanowire Arrays as an Additive-Free Air-Cathode for Flexible Solid-State Zinc-Air Batteries. *Adv. Mater.* **2017**, *29*, 1602868.

- (35) Liu, X.; Xi, W.; Li, C.; Li, X.; Shi, J.; Shen, Y.; He, J.; Zhang, L.; Xie, L.; Sun, X.; Wang, P.; Luo, J.; Liu, L.-M.; Ding, Y. Nanoporous Zn-Doped Co_3O_4 Sheets with Single-Unit-Cell-Wide Lateral Surfaces for Efficient Oxygen Evolution and Water Splitting. *Nano Energy* **2018**, *44*, 371–377.
- (36) Shinagawa, T.; Larrázabal, G. O.; Martín, A. J.; Krumeich, F.; Perez-Ramirez, J. Sulfur-Modified Copper Catalysts for the Electrochemical Reduction of Carbon Dioxide to Formate. *ACS Catal.* **2018**, *8*, 837–844.
- (37) Chu, K.; Wang, F.; Li, Y. B.; Wang, X. H.; Huang, D. J.; Zhang, H. Interface Structure and Strengthening Behavior of Graphene/CuCr Composites. *Carbon* **2018**, *133*, 127–139.
- (38) Chu, K.; Wang, F.; Li, Y. B.; Wang, X. H.; Huang, D. J.; Geng, Z. R. Interface and Mechanical/Thermal Properties of Graphene/Copper Composite with Mo_2C Nanoparticles Grown on Graphene. *Composites, Part A* **2018**, *109*, 267–279.
- (39) Zhang, T.; Wu, M.-Y.; Yan, D.-Y.; Mao, J.; Liu, H.; Hu, W.-B.; Du, X.-W.; Ling, T.; Qiao, S.-Z. Engineering Oxygen Vacancy on NiO Nanorod Arrays for Alkaline Hydrogen Evolution. *Nano Energy* **2018**, *43*, 103–109.
- (40) Chu, K.; Wang, F.; Wang, X. H.; Huang, D. J. Anisotropic Mechanical Properties of Graphene/Copper Composites with Aligned Graphene. *Mater. Sci. Eng., A* **2018**, *713*, 269–277.
- (41) Xu, L.; Jiang, Q.; Xiao, Z.; Li, X.; Huo, J.; Wang, S.; Dai, L. Plasma-Engraved Co_3O_4 Nanosheets with Oxygen Vacancies and High Surface Area for the Oxygen Evolution Reaction. *Angew. Chem., Int. Ed.* **2016**, *55*, 5277–5281.
- (42) Chu, K.; Wang, J.; Liu, Y. P.; Li, Y. B.; Jia, C. C.; Zhang, H. Creating Defects on Graphene Basal-Plane toward Interface Optimization of Graphene/CuCr Composites. *Carbon* **2019**, *143*, 85–96.
- (43) Chu, K.; Wang, J.; Liu, Y. P.; Geng, Z. R. Graphene Defect Engineering for Optimizing the Interface and Mechanical Properties of Graphene/Copper Composites. *Carbon* **2018**, *140*, 112–123.
- (44) Chu, K.; Wang, F.; Wang, X. H.; Li, Y. B.; Geng, Z. R.; Huang, D. J.; Zhang, H. Interface Design of Graphene/Copper Composites by Matrix Alloying with Titanium. *Mater. Des.* **2018**, *144*, 290–303.
- (45) Cui, D.; Zheng, Z.; Peng, X.; Li, T.; Sun, T.; Yuan, L. Fluorine-Doped SnO_2 Nanoparticles Anchored on Reduced Graphene Oxide as a High-Performance Lithium Ion Battery Anode. *J. Power Sources* **2017**, *362*, 20–26.
- (46) Liu, H.; He, Q.; Jiang, H.; Lin, Y.; Zhang, Y.; Habib, M.; Chen, S.; Song, L. Electronic Structure Reconfiguration toward Pyrite NiS_2 via Engineered Heteroatom Defect Boosting Overall Water Splitting. *ACS Nano* **2017**, *11*, 11574–11583.
- (47) Zuo, J.; Xu, C.; Liu, X.; Wang, C.; Wang, C.; Hu, Y.; Qian, Y. Study of the Raman Spectrum of Nanometer SnO_2 . *J. Appl. Phys.* **1994**, *75*, 1835–1836.
- (48) Zhu, D.; Zhang, L.; Ruther, R. E.; Hamers, R. J. Photo-Illuminated Diamond as a Solid-State Source of Solvated Electrons in Water for Nitrogen Reduction. *Nat. Mater.* **2013**, *12*, 836.
- (49) Watt, G. W.; Chrisp, J. D. Spectrophotometric Method for Determination of Hydrazine. *Anal. Chem.* **1952**, *24*, 2006–2008.
- (50) Wu, X.; Xia, L.; Wang, Y.; Lu, W.; Liu, Q.; Shi, X.; Sun, X. Mn_3O_4 Nanocube: An Efficient Electro-catalyst toward Artificial N_2 Fixation to NH_3 . *Small* **2018**, *14*, 1803111.
- (51) Zhu, X.; Wu, T.; Ji, L.; Li, C.; Wang, T.; Wen, S.; Gao, S.; Shi, X.; Luo, Y.; Peng, Q.; Sun, X. Ambient Electrohydrogenation of N_2 for NH_3 Synthesis on Non-Metal Boron Phosphide Nanoparticles: The Critical Role of P in Boosting the Catalytic Activity. *J. Mater. Chem. A* **2019**, *7*, 16117.
- (52) Xian, H.; Wang, Q.; Yu, G.; Wang, H.; Li, Y.; Wang, Y.; Li, T. Electrochemical Synthesis of Ammonia by Zirconia-Based Catalysts at Ambient Conditions. *Appl. Catal., A* **2019**, *581*, 116–122.
- (53) Yu, J.; Li, C.; Li, B.; Zhu, X.; Zhang, R.; Ji, L.; Tang, D.; Asiri, A. M.; Sun, X.; Li, Q.; Liu, S.; Luo, Y. A Perovskite $\text{La}_2\text{Ti}_2\text{O}_7$ Nanosheet as an Efficient Electro-catalyst for Artificial N_2 Fixation to NH_3 in Acidic Media. *Chem. Commun.* **2019**, *55*, 6401–6404.
- (54) Xie, H.; Wang, H.; Geng, Q.; Xing, Z.; Wang, W.; Chen, J.; Ji, L.; Chang, L.; Wang, Z.; Mao, J. Oxygen Vacancies of Cr-Doped CeO_2 Nanorods That Efficiently Enhance the Performance of Electro-catalytic N_2 Fixation to NH_3 under Ambient Conditions. *Inorg. Chem.* **2019**, *58*, 5423–5427.
- (55) Chen, G. F.; Ren, S. Y.; Zhang, L. L.; Cheng, H.; Luo, Y. R.; Zhu, K. H.; Ding, L. X.; Wang, H. H. Advances in Electro-catalytic N_2 Reduction-Strategies to Tackle the Selectivity Challenge. *Small Methods* **2019**, *3*, 1800337.
- (56) Chu, K.; Wang, X. H.; Wang, F.; Li, Y. B.; Huang, D. J.; Liu, H.; Ma, W. L.; Liu, F. X.; Zhang, H. Largely Enhanced Thermal Conductivity of Graphene/Copper Composites with Highly Aligned Graphene Network. *Carbon* **2018**, *127*, 102–112.
- (57) Chu, K.; Wang, X. H.; Li, Y. B.; Huang, D. J.; Geng, Z. R.; Zhao, X. L.; Liu, H.; Zhang, H. Thermal Properties of Graphene/Metal Composites with Aligned Graphene. *Mater. Des.* **2018**, *140*, 85–94.
- (58) Xu, G.; Zhang, L.; He, C.; Ma, D.; Lu, Z. Adsorption and Oxidation of NO on Various SnO_2 Surfaces: A Density Functional Theory Study. *Sens. Actuators, B* **2015**, *221*, 717–722.
- (59) Chu, K.; Liu, Y.; Wang, J.; Zhang, H. NiO Nanodots on Graphene for Efficient Electrochemical N_2 Reduction to NH_3 . *ACS Appl. Energy Mater.* **2019**, *2*, 2288–2295.
- (60) Yu, X.; Han, P.; Wei, Z.; Huang, L.; Gu, Z.; Peng, S.; Ma, J.; Zheng, G. Boron-Doped Graphene for Electro-catalytic N_2 Reduction. *Joule* **2018**, *2*, 1610–1622.